Dual-Polarized mm-Wave Endfire Antenna for Mobile Devices

Resti Montoya Moreno, Juha Ala-Laurinaho, Alexander Khripkov, Janne Ilvonen, and Ville Viikari, *Senior Member, IEEE*

***Abstract*— This article presents a dual-polarized millimeter-wave endfire antenna array for mobile devices. The antenna array is integrated into a metal-framed mobile phone and radiates through a 20 × 3.5 mm^2 window in the metal frame. The measurement results show a realized gain above 6 dBi for the frequency band of 28–33 GHz for a three-element array. Beam-steering up to ±40° is possible. The array is physically offset from the metal frame, thus minimizing the capacitive loading effect on the sub-6 GHz antennas. Moreover, due to the lack of mechanical contact between the frame and the antenna module, the antenna is robust against external impacts or hits to the phone. The design of the antenna module facilitates integration in mobile devices for mm-wave operation.**

***Index Terms*— 5G, antenna, beam-steering, endfire antenna array, metal rim, mm-wave frequencies, smartphone.**

I. Introduction

TRANSMITTED data over cellular networks have been increasing at an exponential rate in recent years. In order to satisfy the needs of future networks, new technical solutions such as high-order multiple-input multiple-output (MIMO) antenna arrays, network densification, broader frequency bands, and higher frequencies will be used [1]. Frequencies in the range of 20–80 GHz concurrently with sub-6 GHz bands are expected to be used in future 5G mobile devices [2]–[4]. Thus, new antenna structures are needed in mobile devices to support the upcoming mm-wave bands. This brings a totally new set of challenges to mobile phone antenna designers. First of all, current mobile devices are tightly packed structures, where the volume reserved for the antennas is extremely small. Second, the majority of current smartphones have a metal frame for robustness and esthetic appearance. On the other hand, directing millimeter-waves in the endfire direction is challenging since the radiation is blocked by the metal frame.

For a reliable connection, angular coverage of mm-wave antennas should be as large as possible. Generally, mm-wave antennas realized on a printed circuit board (PCB) provide good performance toward the broadside direction with respect to the mobile phone [5]. These antennas may also provide dual-polarized operation using, for instance, dual-polarized patch antennas [6], [7]. However, the difficulty in achieving the dual-polarized operation in the endfire direction is considerably more severe. The reason for the increase in difficulty is that the PCB is thin with respect to the wavelength (∼10 mm at 30 GHz), which makes implementing antennas with orthogonal E-fields on the PCB difficult.

Mm-wave antennas must comply with current mobile phone designs. Thus, the antennas should not degrade the visual appearance and mechanical robustness, or significantly increase the manufacturing costs. Moreover, they should not degrade the performance of the sub-6 GHz antennas. Long-term evolution (LTE) antennas of metal-framed phones are typically realized on the metal frame, whose sections act as capacitive coupling elements (CCEs) exciting radiating current distribution on the device [8], [9]. A millimeter-wave antenna module located near the metal frame easily loads the LTE antenna capacitively or may even short-circuit it. Such a scenario would significantly decrease the performance of the LTE antenna, and therefore, any loading of the LTE antenna should be minimized.

Recently, mm-wave antennas for mobile devices have attracted increased interest in the academic community, and several endfire antenna designs have been published in the literature [10]–[24]. Endfire antennas provide good coverage, and generally, radiation is directed neither toward the user nor toward the ground. Kurvinen *et al.* [14] present a combination of both LTE and mm-wave antennas. The proposed antenna presents good performance, but the mm-wave array operates only at a single polarization, and its beam-steering capabilities are only demonstrated in the ±25° range. Furthermore, the effect of the window on different polarizations is not studied. In [15], very good single-polarized performance is achieved in the 27.5–30 GHz range. On the other hand, multiple gaps and slots are needed in the metal frame, which may be impractical. In the design presented in [16], Stanley *et al.* can achieve high gain and wide-angular beam scanning with a combination of three arrays. Even though the prototype includes some of the elements of modern smartphones, a metal frame is not included, and the arrays only provide a single-polarized operation. In [17], a dual-polarized mm-wave array is presented using flexible PCBs and

Manuscript received July 8, 2019; revised February 19, 2020; accepted April 3, 2020. Date of publication April 30, 2020; date of current version August 4, 2020. This work was supported by Huawei Technologies Finland. *(Corresponding author: Resti Montoya Moreno.)*

Resti Montoya Moreno, Juha Ala-Laurinaho, and Ville Viikari are with the Department of Electronics and Nanoengineering, School of Electrical Engineering, Aalto University, 00076 Espoo, Finland (e-mail: resti.montoyamoreno@aalto.fi).

Alexander Khripkov and Janne Ilvonen are with Huawei Technologies Finland, 00180 Helsinki, Finland.

Color versions of one or more of the figures in this article are available online at http://ieeexplore.ieee.org.

Digital Object Identifier 10.1109/TAP.2020.2989556

rod waveguides. However, the array occupies a considerable volume, and only, simulations are presented. A very wide-bandwidth mm-wave antenna is presented in [18], but only, simulation results are shown. In [19], a 28 GHz antenna inside a cellular handset is presented. The design presents good beam-steering capabilities, but it is, as most of the previously mentioned designs, single-polarized, and the mobile phone does not include a metal frame. A multiband endfire array that operates at 28, 38, 48, and 64 GHz is presented in [20]. Even though the concept is very promising, only simulations are shown. In [21], a dual-polarized mm-wave module that is partially integrated into the metal frame is presented. However, the module is not physically offset from the metal frame and, therefore, requires the use of the special feed presented in [25], which may be challenging to produce in a flexible PCB. Furthermore, a shaped window on the metal frame is required. In [22], an interesting endfire design using two subarrays, each one consisting of eight slot antennas, is introduced. However, the bandwidth is relatively narrow, and it presents a single-polarized operation. In [23] and [24], the mm-wave antennas are integrated into the metal frame, and they provide the endfire operation. The first one [23] provides a single-polarized dual-band operation using two differently sized slots in the metal frame. The second design [24] presents the simulation results of a dual-polarized and dual-band patch array. Patch array is a well-known solution, but it could be challenging to integrate into the metal frame, thus depending on the manufacturing technique and design constraints of the device. Moreover, the mm-wave array directly on the metal frame easily short-circuits the LTE antenna, if it is realized on the same metal frame section.

In this article, we present the first experimentally verified endfire mm-wave dual-polarized antenna array that is implemented in a metal-framed mobile phone structure, where the mm-wave module is physically offset from the metal frame. We also study the impact of the window in the metal frame on the two orthogonal polarizations.

The main novelty of the design relies on the implementation of the challenging vertical polarization via capacitive coupling between horizontal transmission lines on a PCB and vertically placed dipoles on a Mylar film, thus avoiding the need for a high-quality galvanic connection or soldering, and the overall packaging of the antenna. The structure of the mobile phone resembles that of a modern smartphone, where a metal frame is usually present and the clearance between the frame and the ground plane is small (1.8 mm). The mm-wave antennas are placed sufficiently far from the metal frame to avoid a short circuit or capacitive loading of the sub-6 GHz antennas implemented in it. The feedlines include a two-step balun transition that transforms the unbalanced signal from the connector into a balanced one that feeds each element of the array. Radiation is directed out of the phone through a small window in the metal frame. The proposed design presents the following benefits.

1) The antenna can coexist with sub-6 GHz antennas since the necessary shaping of the metal frame does not considerably degrade the low-band (LB) antenna (700–960 MHz) performance, and the mm-wave module is placed 1 mm away from the metal frame.
2) The absence of a mechanical or electrical contact between the frame and the antenna module makes it robust against impacts.
3) The presented solution supports dual-polarized beamforming.
4) This solution provides an endfire array pattern, which is essential to complement the 3-D scanning coverage.

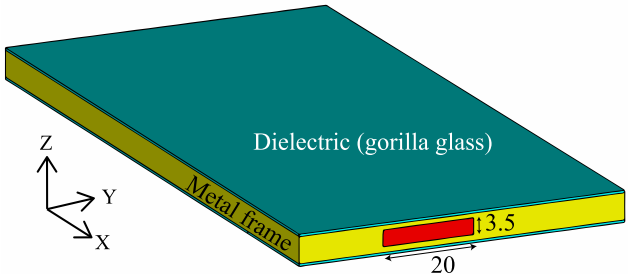

Fig. 1. Front view of the antenna (outside of the mobile device). Dimensions are in mm.

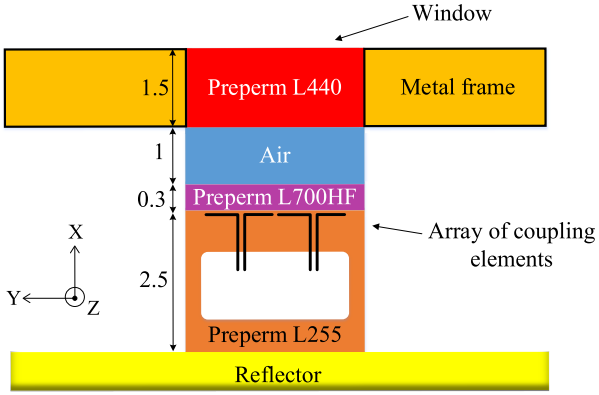

Fig. 2. Schematic of the plastic structure used in the design and their thicknesses in mm. The figure is not to scale.

This article is organized as follows. Section II presents the mm-wave antenna concept and feeding structure alongside the main antenna dimensions and plastic materials used. The simulation and measurement results are presented, compared, and analyzed in Section III. Section IV analyzes the results and clarifies the differences between the simulated and measured structures. Section V presents a tolerance study of the main elements affecting the antenna performance. Finally, conclusions are presented in Section VI.

II. Antenna Design

A. mm-Wave Antenna

Fig. 1 shows the outer view of the simulated phone model. The phone includes a window in the metal frame (3.5×20 mm^2) in order to enable radiation toward the endfire direction. Fig. 2 shows the distribution of the main elements in the proposed antenna concept. The main antenna elements

TABLE I
MAIN DIELECTRIC PROPERTIES

Material	Description	ϵ_r	tan δ
Preperm L440	Plastic used to fill the window in the metal frame	4.6	0.005
Preperm L700HF	Superstrate	7.0	0.005
Preperm L255	Supporting plastic for reflector	2.55	0.005
Rogers 4350B	PCB substrate	3.66	0.005

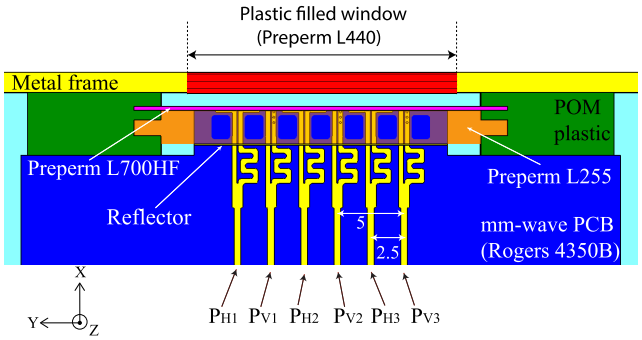

Fig. 3. Top view of the proposed antenna as seen from inside the phone. The metallic unibody of the phone is hidden, and the plastic L255 is partially transparent. Dimensions are in mm.

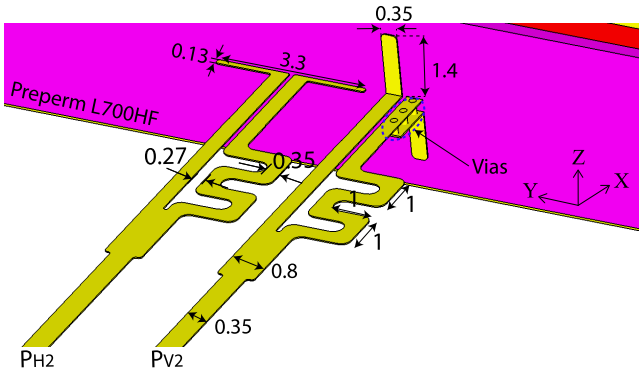

Fig. 4. mm-wave antennas, placed next to the high-permittivity plastic layer Preperm L700HF. The V-pol feedlines are guided toward the bottom using vias. Dimensions are in mm. The PCB and some other parts are removed for clarity.

of the mm-wave module are the back reflector, the coupling elements, the superstrate layers, and the window in the metal frame. Table I summarizes the main electrical properties of all the dielectrics used in the antenna design.

Fig. 3 shows the proposed antenna structure seen from inside the phone (top view). First, a reflector isolates the antenna from the other metallic parts inside the phone. The reflector is ideally placed at a distance of $\lambda/4$ for maximum directivity of the antenna elements. For the horizontally polarized elements, the ground plane of the PCB partially behaves as the reflector, such as the one used in Yagi–Uda antennas. For the vertically polarized antennas, the inclusion of a vertically oriented reflector is necessary in order to achieve a more directive pattern.

As shown in Fig. 4, the primary coupling elements are horizontally and vertically polarized (H-pol and V-pol) dipoles. Each array consists of three elements, and hence, every element is used for a different polarization.

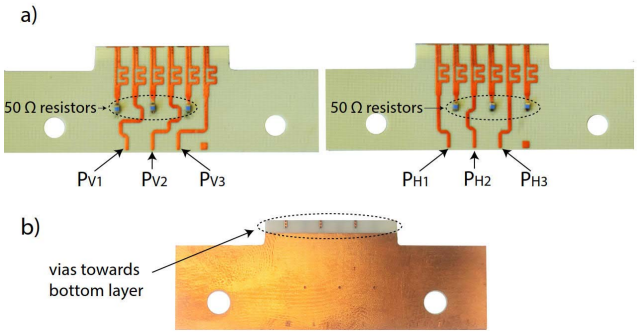

Fig. 5. Prototyped vertically and horizontally polarized antenna PCBs. (a) Top view. (b) Bottom view.

In order to enhance the radiation properties of the chosen coupling elements, a high-permittivity plastic layer is added next to them. In addition, the layer of Preperm L700HF plastic ($\epsilon_r = 7$, tan $\delta = 0.005$) allows the reduction of the dimension of the V-pol and H-pol antennas and also enhances radiation toward the window in the metal frame. The use of one or more high-permittivity dielectrics as superstrates in order to enhance the properties of antennas manufactured on PCBs has been extensively studied in the literature [26]–[31]. Generally, there is a tradeoff between operational bandwidth and maximum directivity. Multilayered superstrate designs may enhance the operational bandwidth. However, although, with these superstrates, the directivity drops slightly, a thicker structure is required.

Finally, a window in the metal frame is necessary to direct the energy from the main couplers toward the endfire direction. Moreover, this window is filled with the dielectric Preperm L440 ($\epsilon_r = 4.6$, tan $\delta = 0.005$), thus creating a multilayered superstrate structure.

B. Prototype Considerations

A prototype was manufactured to verify the concepts presented in Section II-A. The antenna is designed so that it is fed from an integrated multichannel phase-shifter chip. However, for characterization purposes, the array elements are fed separately through coaxial connectors. Due to the relatively large connector size, two PCBs were designed, one to feed the horizontally polarized array and the other for the vertically polarized array. Each PCB consists of two metal layers and one Rogers 4350B substrate layer of thickness 0.254 mm. Hence, the two PCBs must be interchanged in order to measure different polarizations. Nonetheless, all the antenna elements are included on both PCBs, and thus, the nonfed elements are terminated with 50 Ω resistors, as shown in Fig. 5. As seen from these figures, the horizontally polarized dipoles are implemented directly on the PCBs since they are on the same plane, whereas the vertically polarized dipole arms are oriented perpendicular to the PCB surface.

As shown in Figs. 4 and 5, the V-pol feedlines extend to the end of the PCB, where one of the two balanced feedlines is guided to the bottom side of the PCB using three vias. The vertical dipoles and the reflector are built from copper on

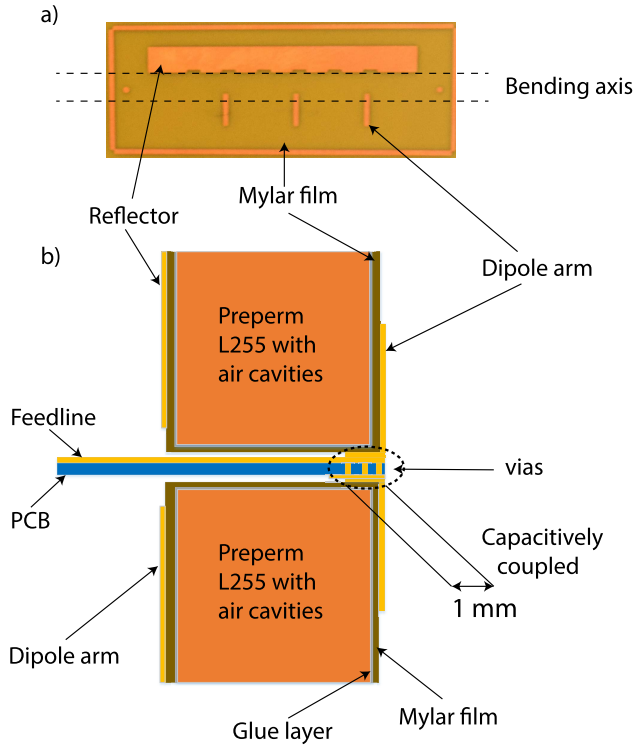

Fig. 6. (a) Vertical dipoles and reflector implemented on a Mylar film. (b) Mylar films bent around the two supporting L255 plastic.

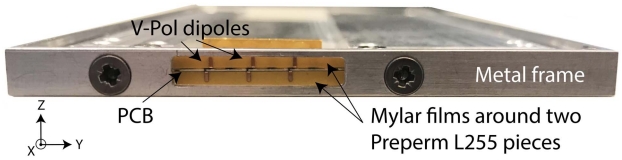

Fig. 7. Front view of the prototyped mobile phone model. The plastics L700HF and L440 are not shown.

a mylar film (see Fig. 6). The mylar film is bent up and down around two L255 plastic pieces, as shown in Figs. 6 and 7: one on the top and the other underneath the PCB. The vertical dipoles are capacitively coupled to the balanced lines in an area of 1×0.35 mm^2, thus avoiding the need for any soldering. In the simulation model, the gap between the capacitively coupled V-pol dipole arm and the feedline is assumed to be zero. A tolerance analysis of this distance is presented in Section V.

The dipoles are balanced structures, and thus, they require the inclusion of a balanced-to-unbalanced (balun) transition to make it compatible with most RF measurement devices. Different balun transitions have been studied in the past years [32]–[36], some of which require a relatively long tapering of the ground plane or a wide meandered section. In this solution, a variation of the balun presented in [37] is proposed. Since the spacing between the cross-polarized antenna elements is only 2.5 mm, the 180° phase shift in one of the arms is performed in two steps. This way, the width of the balun is reduced sufficiently to fit in the limited space, as shown in Fig. 5. Compared to the standard solution, the proposed balun presents similar performance when implemented

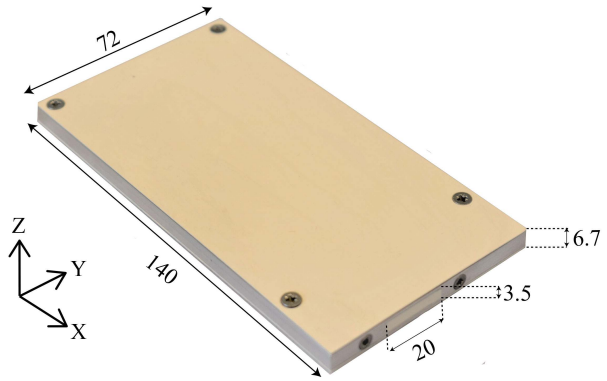

Fig. 8. Prototyped mobile phone model. Dimensions are in mm.

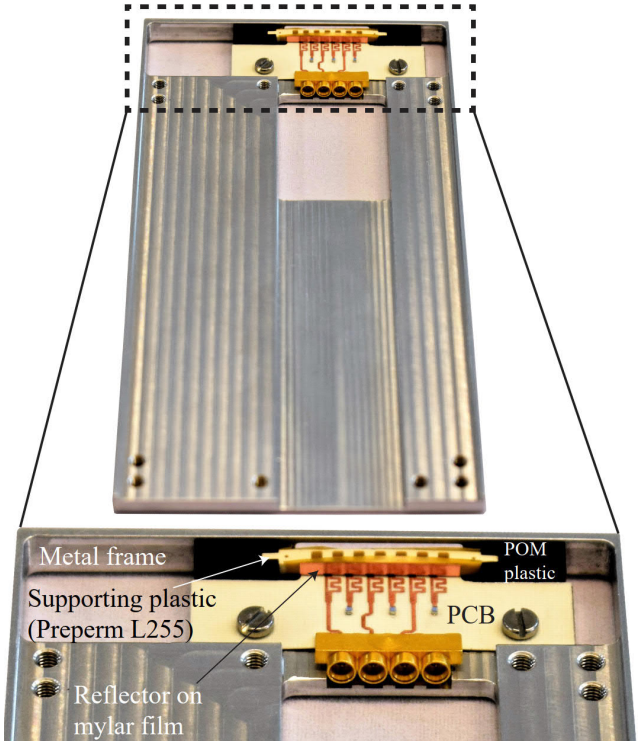

Fig. 9. Tilted top view of the prototyped mobile phone model. The dielectric on the top and the metal cover are removed to show the mm-wave module.

in a Rogers 4350B substrate ($\epsilon_r = 3.66$, $\tan\delta = 0.005$) since the insertion loss (IL) in the frequency band of operation (24–30 GHz) remains below 1 dB for both solutions.

The prototype, which can be seen in Figs. 8 and 9, is formed by the PCBs, the SMPM edge-launch connectors, the metal body of the phone, the top and bottom glass, the shaped POM plastic, and the superstrate. The two pieces of POM plastic are screwed to the metal frame in the antenna assembly, and they are shaped to keep the supporting L255 plastic ($\epsilon_r = 2.55$, $\tan\delta = 0.005$) and the superstrate L700HF layer in place. The dimensions of the prototype are $140 \times 72 \times 6.7$ mm^3, which are in agreement with the size of current smartphones.

In order to compare the simulated and measured values, two simulation models of the PCB are built, of which the first model has three simulation ports that feed the horizontally polarized antennas when the vertically polarized antennas are

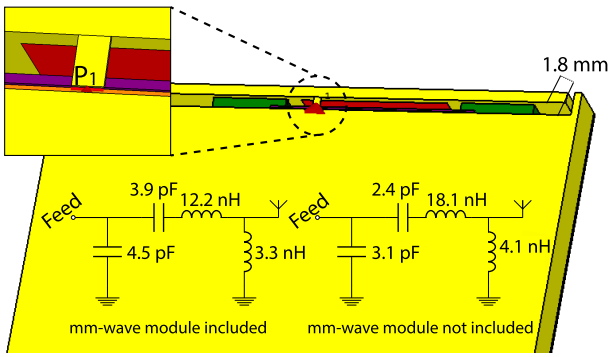

Fig. 10. Simulation model of the LB antenna, and the desired matching circuits for the device with and without the mm-wave module. Feed port is shown in the zoomed-in view photograph.

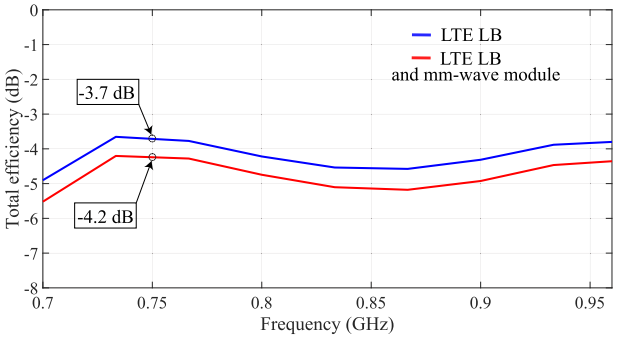

Fig. 11. Total efficiency of the LB antenna with and without the mm-wave module.

terminated with 50 Ω resistors and the second model similarly feeds the vertically polarized antennas when the horizontally polarized antennas are terminated.

The simulated reflection coefficient is below −10 dB between 24 and 30 GHz for the H-Pol and between 26.5 and 30 GHz for the V-Pol. The simulated peak realized gain for the three-element array including the feedlines is above 4.5 dBi for the frequency range of 24–30 GHz and above 6 dBi between 26 and 30 GHz.

C. LTE LB Antenna

In order to quantify the effect of the mm-wave module on the sub-6 GHz antennas, an LTE LB antenna is simulated. As explained in Section I, both LTE and mm-wave antennas must coexist in future 5G smartphones, thus implying that one antenna must not deteriorate the performance of the other. The LB antenna is designed using a CCE implementation integrated into the metal frame to operate in the 700–960 MHz band. First, the LB antenna is optimized for a reasonable performance when the mm-wave module is not included; then, the mm-wave module is added to the model and the matching network is recalculated in the matching network optimization tool Optenni Lab. The simulated antenna structure and both matching circuits are shown in Fig. 10. Both matching circuits share the same topology, and only, the component values are reoptimized. The LB antenna feed is placed in the middle of the metal frame. Fig. 11 shows the comparison of the total

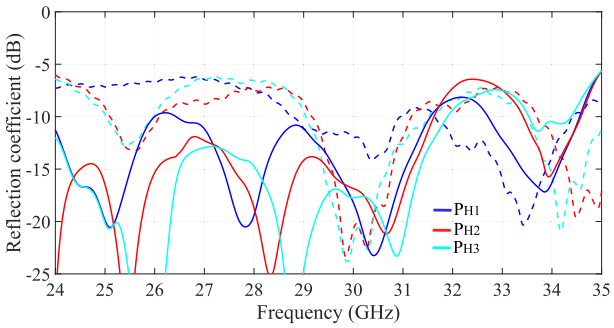

Fig. 12. Reflection coefficient of the horizontally polarized antennas. Solid lines: simulated values. Dashed lines: measured values.

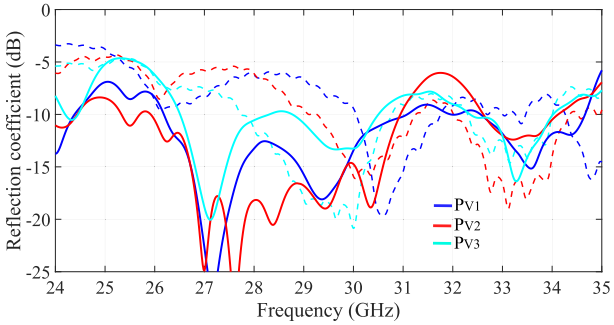

Fig. 13. Reflection coefficient of the vertically polarized antennas. Solid lines: simulated values. Dashed lines: measured values.

efficiency for both models with and without the mm-wave module. As can be seen, introducing the mm-wave module decreases the total performance of the LB antenna by less than 0.5 dB. Thus, the effect of the mm-wave module is much smaller than a solution that would short-circuit the metal frame. The LTE LB antenna described in this section is not included in the prototype.

III. Measurement Results

This section presents the measured results and compares them with the simulation results. As a result of the available measurement setup, each antenna port is measured individually. The three-element array results, i.e., realized gain and radiation pattern, presented in this section have been obtained by combining the individually measured, port-specific results in MATLAB.

An SMPM male edge-launch connector is used to feed each PCB, and the nonfed elements are terminated with 50 Ω resistors. Since only four-port connectors were available, the right-most connector port is grounded.

Figs. 12 and 13 show the comparison of the simulated and measured reflection coefficient for the horizontally and vertically polarized elements, respectively. The simulated matching level is below −10 dB in the 26.5–30.5 GHz band for both polarizations. However, the measured S-parameters show a frequency shift. Therefore, the measured matching level is below −8 dB in the 29–35 GHz band. The simulated isolation between different polarizations is 15 dB at worst and can be generally found above 20 dB.

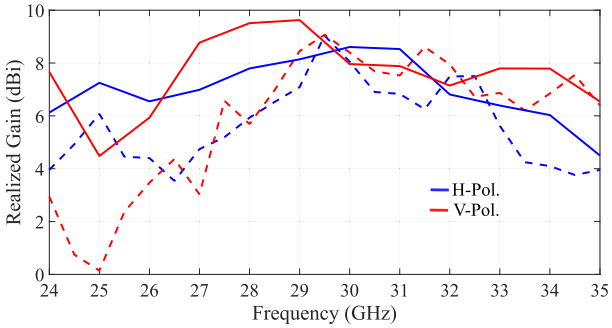

Fig. 14. Measured and simulated peak realized gain for the three-element arrays. Solid lines: simulated values. Dashed lines: measured values.

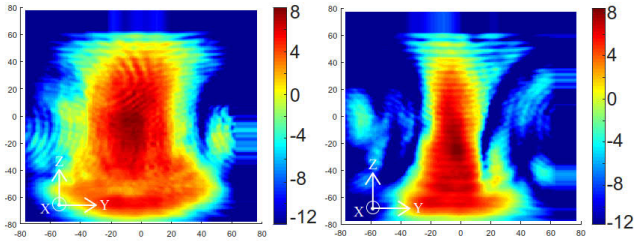

Fig. 15. Measured radiation pattern of the three-element array at 30 GHz for horizontal and vertical polarizations in the broadside direction, respectively. Realized gain values are in dBi.

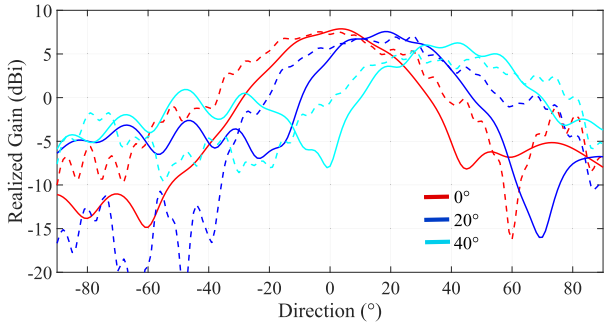

Fig. 16. Realized gain radiation pattern of the three-element antenna array at 30 GHz for the horizontal polarization. Solid lines: simulated values. Dashed lines: measured values.

The peak realized gain versus frequency for the three-element array is presented in Fig. 14. The measured and simulated realized gain is above 6 dBi for the 28–33 GHz band and peaks at 9 dBi for both polarizations. In the 24–26 GHz range, there is a considerable discrepancy between the simulated and measured peak realized gain values, which is caused due to a distorted individual beam pattern. Reasons for this are given in Section IV. The measured radiation pattern for the three-element array for both polarizations in the broadside direction at 30 GHz is presented in Fig. 15. Since the main goal of mm-wave endfire arrays is to complement broadside arrays for 3-D coverage, the beam-steering capabilities of the array are of major importance. Beam-steering capabilities at 30 GHz are presented in Figs. 16 and 17. These figures have been obtained in MATLAB by phasing each individually measured antenna to maximize the radiated power to the desired direction. Beam-steering up to $\pm 40°$ is possible for the horizontal and vertical polarizations with a scan loss close to 3 dB. According to the simulations, a strong sidelobe

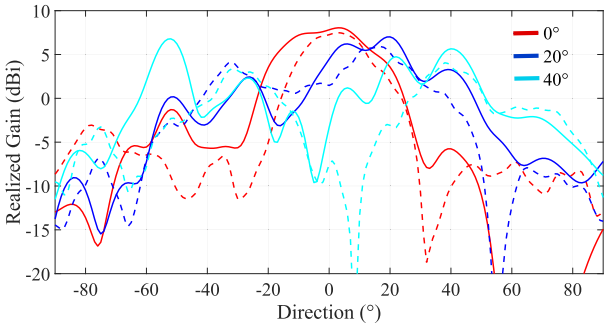

Fig. 17. Realized gain radiation pattern of the three-element antenna array at 30 GHz for the vertical polarization. Solid lines: simulated values. Dashed lines: measured values.

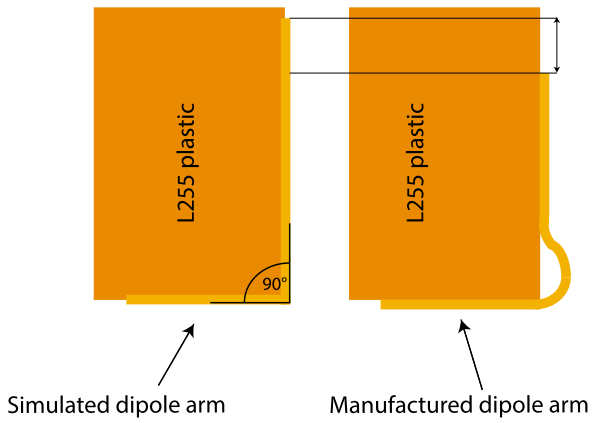

Fig. 18. Simulated dipole arm (left) and the shorter imperfectly bent prototyped dipole arm (right). The figure is not to scale.

appears at $-50°$ when the beam is steered to $+40°$, but the effect is not seen in the measurements. We believe that this difference is caused by slightly different positions of the array with respect to the window, which affects the individual patterns.

As Section V will show in more detail, the window size is the main factor restricting the beam-steering capabilities of the antenna. We kept the window dimensions as small as possible in order to make the design practically feasible.

IV. Measurement Versus Simulation of the Refined Model

In Section III, the simulated and measured results of the antenna performance were compared. This comparison shows that the pattern shape and beam-steering capabilities are in good agreement. However, the peak realized gain is below the simulated target in the 24–28 GHz range. The main reason for this drop is the lower matching efficiency in this frequency range. In this section, we aim to explain the possible reasons for the frequency shift in the S-parameters presented in Figs. 12 and 13.

A careful examination of the prototype indicated some key differences between the prototyped and simulated structures. First of all, the Mylar film included a 25–50 μm thicker than the expected glue layer. Moreover, in the assembly process, the Mylar could not be sharply bent to 90°, but

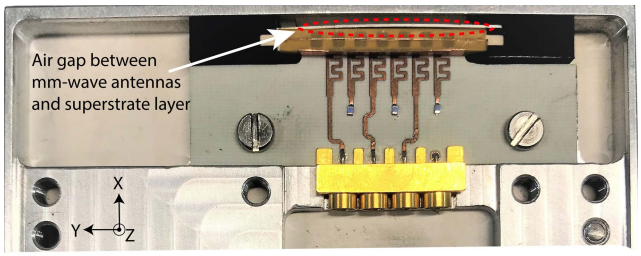

Fig. 19. Prototyped structure. The superstrate layer is not directly in contact with the mm-wave antennas.

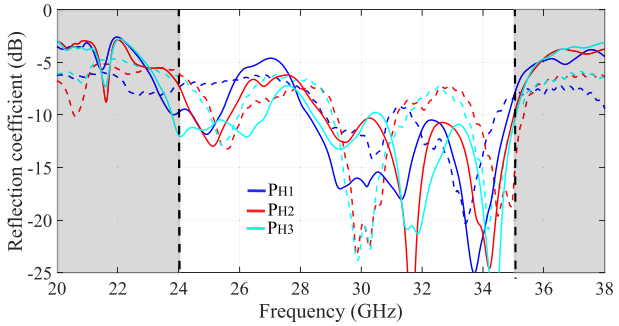

Fig. 20. Reflection coefficient of the horizontally polarized antennas when the simulation model is modified to match the prototyped structure. Solid lines: simulated values. Dashed lines: measured values.

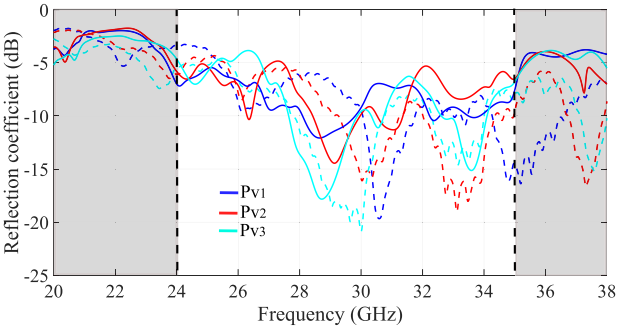

Fig. 21. Reflection coefficient of the vertically polarized antennas when the simulation model is modified to match the prototyped structure. Solid lines: simulated values. Dashed lines: Measured values.

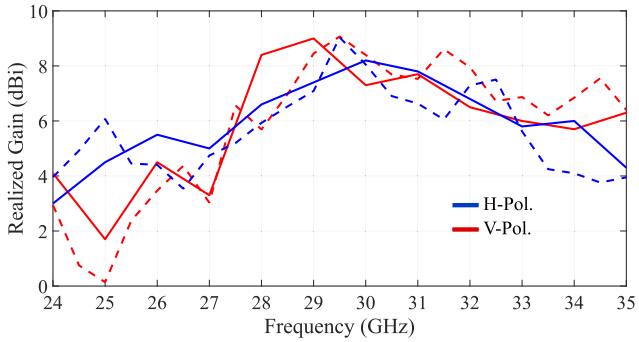

Fig. 22. Measured and simulated peak realized gain for the three-element arrays when the simulation model is modified to match the prototyped structure. Solid lines: simulated values. Dashed lines: measured values.

instead formed a small bending radius (Fig. 18). In addition to the glue layer, this radius made the vertical dipoles slightly shorter, thus shifting the operation toward higher frequencies. Another key difference between the simulated and prototyped

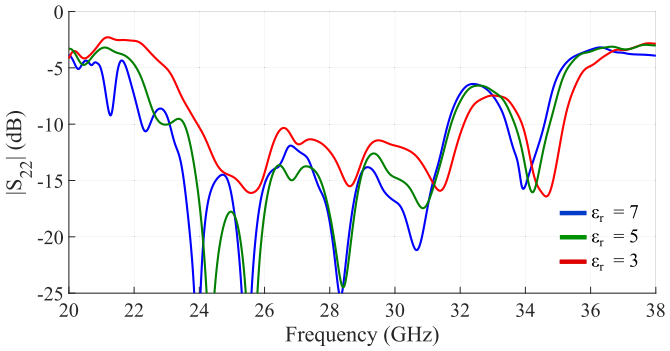

Fig. 23. Reflection coefficient of the horizontally polarized antenna PH2 as a function of frequency. Different curves are for different permittivity values of Preperm L700HF.

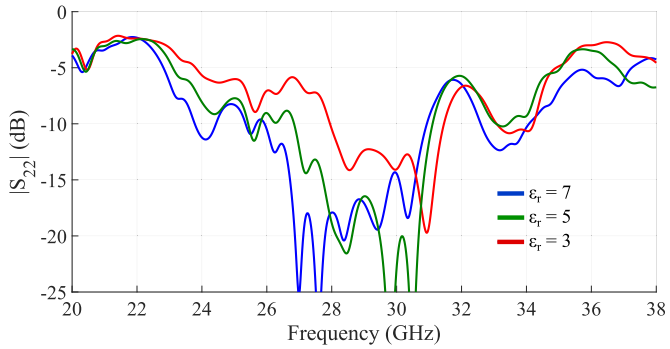

Fig. 24. Reflection coefficient of the vertically polarized antenna PV2 as a function of frequency. Different curves are for different permittivity values of Preperm L700HF.

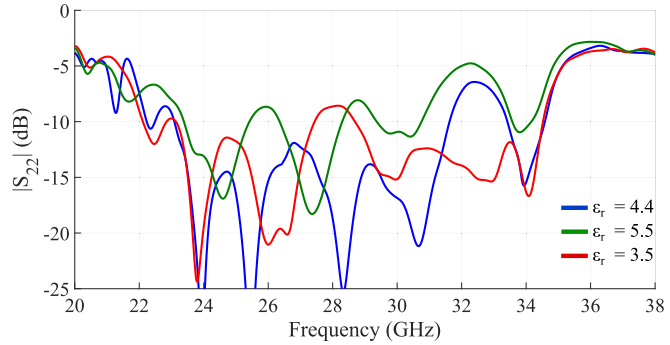

Fig. 25. Reflection coefficient of the horizontally polarized antenna PH2 as a function of frequency. Different curves are for different permittivity values of Preperm 440.

structures is the position of the superstrate layer. In the simulations, this layer is perfectly straight and directly touching the mm-wave antennas, whereas, in the prototype, the layer is partially bent and slightly separated from the antennas (Fig. 19). Precisely quantifying some of these dimensions is not possible. Nonetheless, the simulations show that even small modifications in critical parts of the simulation model can have a considerable effect on the matching.

Taking into account the findings in the prototype, a new simulation model was built. In the new model, the superstrate layer is separated 0.1 mm from the antennas, the vertically polarized dipoles are 0.1 mm shorter to account for the

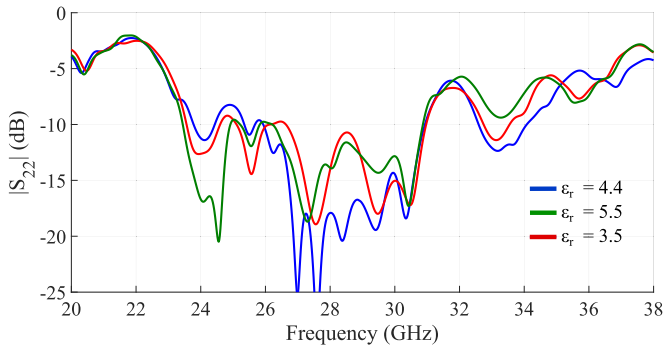

Fig. 26. Reflection coefficient of the vertically polarized antenna PV2 as a function of frequency. Different curves are for different permittivity values of Preperm 440.

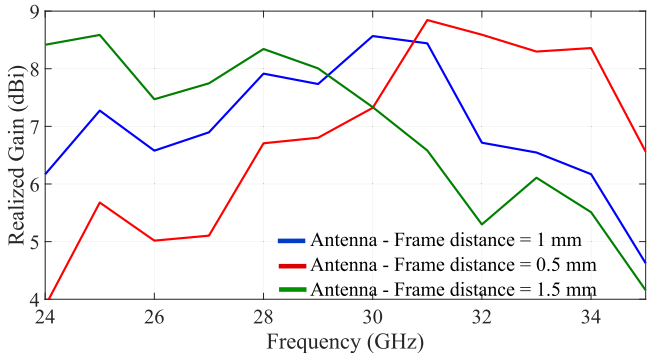

Fig. 27. Simulated maximum realized gain for different distances between the mm-wave antenna and the metal frame for the horizontally polarized antennas.

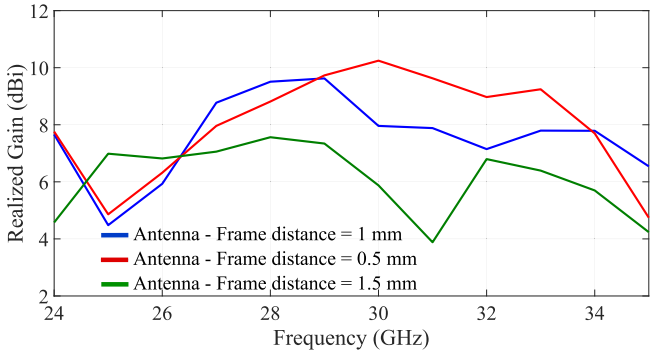

Fig. 28. Simulated maximum realized gain for different distances between the mm-wave antenna and the metal frame for the vertically polarized antennas.

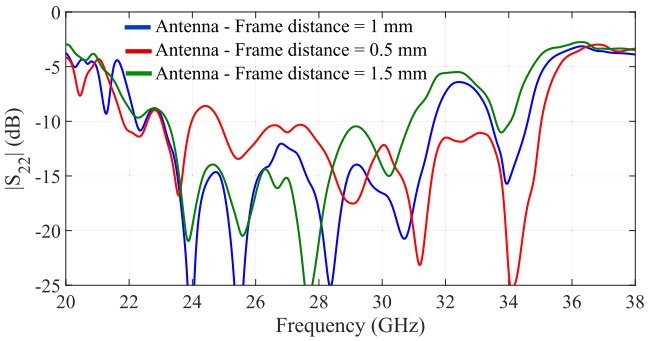

Fig. 29. Reflection coefficient of the horizontally polarized antenna PH2 as a function of frequency. Different curves are for different distances between the mm-wave antenna and the metal frame.

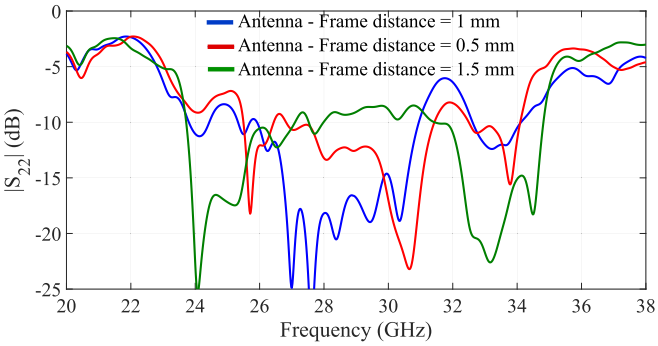

Fig. 30. Reflection coefficient of the vertically polarized antenna PV2 as a function of frequency. Different curves are for different distances between the mm-wave antenna and the metal frame.

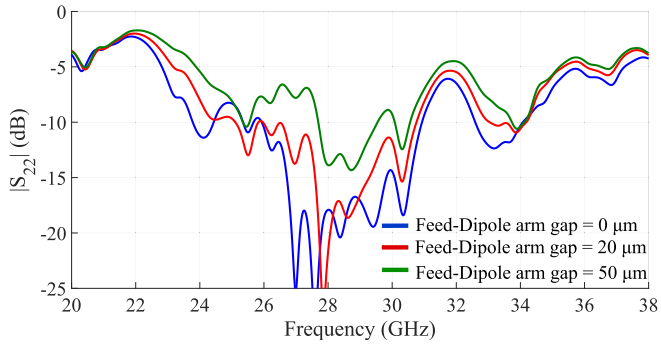

Fig. 31. Reflection coefficient of the vertically polarized antenna PV2 as a function of frequency. Different curves are for different distances between the feed line and the V-pol dipole arm.

bending radius of the Mylar film, and a 0.1 mm glue layer is added between the L255 material and the dipole arm. Figs. 20 and 21 show the matching level for the simulated modified structure and compare it with the measured results. A far better agreement between the simulation and measurement results can be seen from these figures for the entire frequency range of 20–38 GHz. Moreover, Fig. 22 shows the comparison of the peak realized gain of the new simulation model to the measurement results. As shown in Fig. 22, there is also a good agreement between the simulated and measured results, even in the 24–26 GHz range. The authors believe that these are the reasons why the performance of the initial simulated model and the prototyped structure was different.

V. Tolerance Analysis

This section explains how some of the most important elements of the design affect the performance of the mm-wave antenna. The studied parameters are the permittivity of the superstrate layer (Preperm L700HF), the permittivity of the plastic inside the metal frame (Preperm L440), the window dimensions, and the distance between the mm-wave antenna and the metal frame. Since we have multiple optimization goals, such as efficiency, impedance band, and the

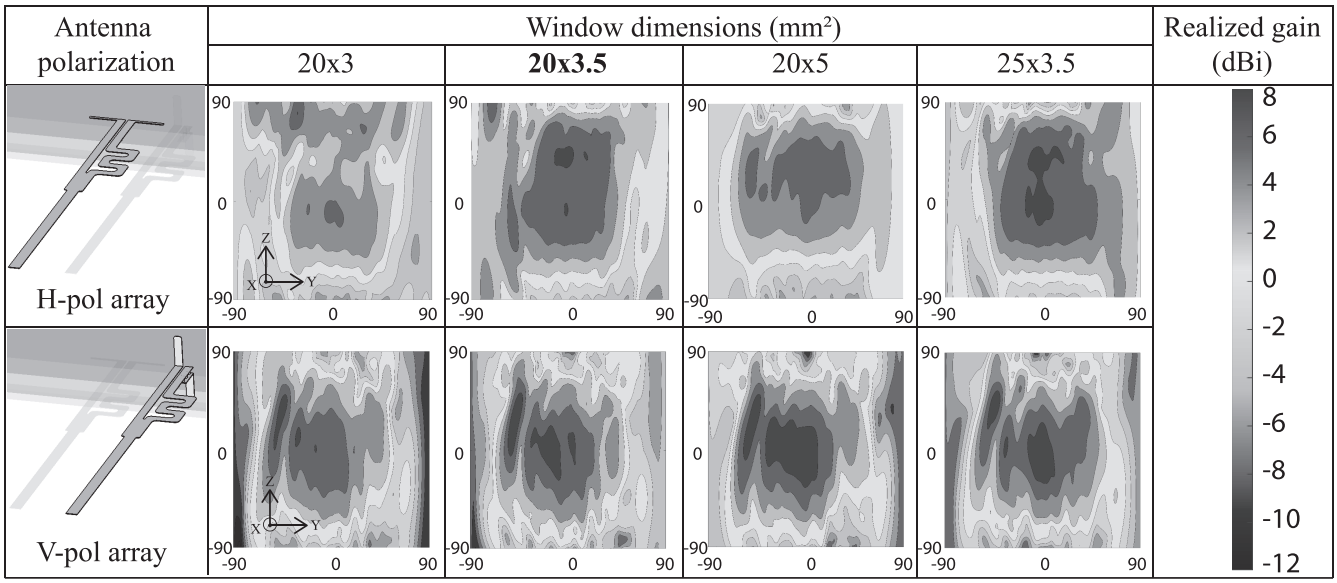

Fig. 32. Envelope radiation pattern when the beam is steered ±90° for horizontal and vertical polarizations at 30 GHz for different window sizes. 20×3.5 mm^2 used in the manufactured prototype.

beam-steering range for both polarizations, making straightforward conclusions about optimal parameter values is often challenging. The blue curves in Figs. 23–31 are the reference results.

A. Superstrate and Window Materials

The layer of high-permittivity plastic allows reducing the dipole dimensions and focusing the beam toward the endfire direction. Figs. 23 and 24 show the reflection coefficient as a function of frequency for different substrate permittivities. The sweep, which focuses on the performance of the middle ports PV2 and PH2, shows that when the permittivity is not large enough, the matching worsens rapidly. The vertically polarized antennas are, as shown in the figures, more sensitive to the superstrate layer.

On the other hand, the plastic filling of the window in the metal frame (Preperm L440) heavily affects the horizontally polarized antennas, whereas its effect on the vertical ones is not so severe (see Figs. 25 and 26). One of the reasons for this behavior is that when the permittivity decreases, the dimensions of the window effectively decrease. In this case, if the metal frame is sufficiently thick, it behaves as a waveguide, and therefore, the cutoff frequency close to the operating frequency starts to heavily affect the performance. On the other hand, when the permittivity increases, the distance of the window from the antenna is not optimal, and the layer begins to reflect part of the energy. This could be mitigated by optimizing the distance between the antenna and the window.

B. Distance Between the mm-Wave Antenna and the Metal Frame

In this section, we present the antenna performance when the distance from the mm-wave antenna to the metal frame is varied. One must note that varying this distance will modify not only the performance of the mm-wave antennas but also the capacitive loading of the sub-6 GHz antennas. Therefore, placing the mm-wave module closer to the metal frame will result in deterioration in the performance of the LTE antennas. In this section, we focus only on the performance of the mm-wave antenna. Figs. 27 and 28 show the maximum realized gain when the distance between the mm-wave antennas and the metal frame is varied from 0.5 to 1.5 mm. For the horizontally polarized antennas, varying the distance translates into shifting the optimal frequency of the design. This way, a shorter distance makes the array to operate optimally at higher frequencies, while a longer one provides better performance at lower frequencies. For the vertically polarized antennas, placing the antenna closer to the metal frame slightly increases the realized gain in the upper part of the frequency band. The same trend can be seen from the S-parameters shown in Figs. 29 and 30. The field radiated from the antenna experiences a discontinuity at the window and the surfaces of the plastic block. As a consequence, there is a small standing wave that affects the impedance and radiation properties of the antenna. The standing wave is sensitive to frequency and physical dimensions.

C. Capacitive Coupling Between Feedline and V-Pol Dipole Arm

As it was explained in Section II and illustrated in Fig. 6, the V-pol feedline and antenna are capacitively coupled. The distance between the two is assumed to be zero in the simulations. However, in practice, there might be a small air gap. Fig. 31 shows the comparison of the reflection coefficient for the port PV2 for different gap values. The design tolerates up to 20 μm air gap without a significant change in the impedance. According to the simulations, matching deteriorates when the gap is 50 μm or larger. The antenna could possibly be made less sensitive to the gap by increasing the

overlapping surface area of the feed line and the dipole arm. The larger area should result in larger capacitance and, thus, stronger coupling.

D. Window Dimensions

The dimensions of the window directly affect the achievable beam-steering range. The larger the opening, the better is the antenna performance. However, a small window is preferred for esthetical reasons and robustness. We studied how the window size affects the antenna performance. Fig. 32 shows the envelope patterns (the largest realized gain) for both arrays with different window sizes as a function of the beam-steering angle. For the horizontal polarization, the height of the window is critical in order to achieve a wide beam-steering range. When the window height is 3 mm, the beam-steering range is clearly smaller than that with 3.5 and 5 mm heights. However, a 3.5 mm high window provides almost the same range as a 5 mm high window. The vertical polarization seems to be more robust to different window dimensions. Angular coverage defined by 5 dBi gain is almost the same for all windows, but larger windows provide slightly larger maximum gain at small angles (near broadside). Since the three-element arrays and the window are not symmetric with respect to the phone, the beam-steering range is not fully symmetric. The results indicate that the window size is, as expected, a critical element for the antenna performance, and thus, its size and filling materials should be taken into account already in the early design stages.

VI. Conclusion

This article presents a 5G mm-wave endfire three-element phased-array antenna inside a metal-framed mobile phone. Implementing a dual-polarized endfire antenna array inside a metal-framed model is a challenging task. The measured realized gain is above 6 dBi in the 28–33 GHz band, and beam-steering up to $\pm 40^\circ$ is possible with a scan loss close to 3 dB. Moreover, the mm-wave module is physically offset from the metal frame, where sub-6 GHz antennas are generally implemented, thus not shorting it or degrading its performance more than 0.5 dB based on the performed simulations. The presented antenna array, if combined with a dual-polarized broadside mm-wave antenna, can provide 3-D coverage at mm-wave frequencies.

Acknowledgment

The authors would like to thank Eino Kahra and Antti Kuhlberg for their help in manufacturing and assembling the prototype.

References

[1] S. Andreev, "Delivering uniform connectivity and service experience to converged 5G wireless networks," in *Proc. IEEE World Forum Internet Things (WF-IoT)*, Mar. 2014, pp. 323–324.

[2] *View on 5G Architecture, Version 2.0*, document, 5G PPP Architecture Working Group, 2017. [Online]. Available: https://5g-ppp.eu/wp-content/uploads/2017/07/5G-PPP-5G-Architecture-White-Paper-2-Summer-2017_For-Public-Consultation.pdf

[3] *5G Spectrum*, Public Policy Position, Huawei, Shenzhen, China, 2018.

[4] *Looking Ahead to 5G*, Nokia, Espoo, Finland, 2014.

[5] M. Khalily, R. Tafazolli, P. Xiao, and A. A. Kishk, "Broadband mm-wave microstrip array antenna with improved radiation characteristics for different 5G applications," *IEEE Trans. Antennas Propag.*, vol. 66, no. 9, pp. 4641–4647, Sep. 2018.

[6] J.-K. Du *et al.*, "Dual-polarized patch array antenna package for 5G communication systems," in *Proc. 11th Eur. Conf. Antennas Propag. (EUCAP)*, Mar. 2017, pp. 3493–3496.

[7] H. Xia, T. Zhang, L. Li, and F.-C. Zheng, "A low-cost dual-polarized 28 GHz phased array antenna for 5G communications," in *Proc. Int. Workshop Antenna Technol. (iWAT)*, Mar. 2018, pp. 1–4.

[8] R. Valkonen, M. Kaltiokallio, and C. Icheln, "Capacitive coupling element antennas for multi-standard mobile handsets," *IEEE Trans. Antennas Propag.*, vol. 61, no. 5, pp. 2783–2791, May 2013.

[9] J. Villanen, J. Ollikainen, O. Kivekas, and P. Vainikainen, "Coupling element based mobile terminal antenna structures," *IEEE Trans. Antennas Propag.*, vol. 54, no. 7, pp. 2142–2153, Jul. 2006.

[10] M. M. S. Taheri, A. Abdipour, S. Zhang, and G. F. Pedersen, "Integrated millimeter-wave wideband end-fire 5G beam steerable array and low-frequency 4G LTE antenna in mobile terminals," *IEEE Trans. Veh. Technol.*, vol. 68, no. 4, pp. 4042–4046, Apr. 2019.

[11] R. Rodriguez-Cano, S. Zhang, K. Zhao, and G. F. Pedersen, "Reduction of main beam-blockage in an integrated 5G array with a metal-frame antenna," *IEEE Trans. Antennas Propag.*, vol. 67, no. 5, pp. 3161–3170, May 2019.

[12] W. Hong, K.-H. Baek, and S. Ko, "Millimeter-wave 5G antennas for smartphones: Overview and experimental demonstration," *IEEE Trans. Antennas Propag.*, vol. 65, no. 12, pp. 6250–6261, Dec. 2017.

[13] J. Zhang, K. Zhao, L. Wang, S. Zhang, and G. F. Pedersen, "Dual-polarized phased array with end-fire radiation for 5G handset applications," *IEEE Trans. Antennas Propag.*, vol. 68, no. 4, pp. 3277–3282, Apr. 2020.

[14] J. Kurvinen, H. Kähkönen, A. Lehtovuori, J. Ala-Laurinaho, and V. Viikari, "Co-designed mm-wave and LTE handset antennas," *IEEE Trans. Antennas Propag.*, vol. 67, no. 3, pp. 1545–1553, Mar. 2019.

[15] B. Yu, K. Yang, C.-Y.-D. Sim, and G. Yang, "A novel 28 GHz beam steering array for 5G mobile device with metallic casing application," *IEEE Trans. Antennas Propag.*, vol. 66, no. 1, pp. 462–466, Jan. 2018.

[16] M. Stanley, Y. Huang, H. Wang, H. Zhou, A. Alieldin, and S. Joseph, "A capacitive coupled patch antenna array with high gain and wide coverage for 5G smartphone applications," *IEEE Access*, vol. 6, pp. 41942–41954, 2018.

[17] R. M. Moreno, J. Ala-Laurinaho, and V. Viikari, "Rod waveguides as future 5G antennas for mobile devices," in *Proc. 48th Eur. Microw. Conf. (EuMC)*, Sep. 2018, pp. 1081–1084.

[18] N. O. Parchin, M. Shen, and G. F. Pedersen, "End-fire phased array 5G antenna design using leaf-shaped bow-tie elements for 28/38 GHz MIMO applications," in *Proc. IEEE Int. Conf. Ubiquitous Wireless Broadband (ICUWB)*, Oct. 2016, pp. 1–4.

[19] W. Hong, K. Baek, Y. Lee, and Y. G. Kim, "Design and analysis of a low-profile 28 GHz beam steering antenna solution for future 5G cellular applications," in *IEEE MTT-S Int. Microw. Symp. Dig.*, Jun. 2014, pp. 1–4.

[20] R. Rodríguez-Cano, S. Zhang, and G. F. Pedersen, "Beam-steerable multi-band mm-wave bow-tie antenna array for mobile terminals," in *Proc. 12th Eur. Conf. Antennas Propag. (EuCAP)*, 2018, pp. 1–4.

[21] R. M. Moreno *et al.*, "Dual-polarized mm-wave end-fire chain-slot antenna for mobile devices," *IEEE Trans. Antennas Propag.*, to be published.

[22] J. Bang and J. Choi, "A SAR reduced mm-wave beam-steerable array antenna with dual-mode operation for fully metal-covered 5G cellular handsets," *IEEE Antennas Wireless Propag. Lett.*, vol. 17, no. 6, pp. 1118–1122, Jun. 2018.

[23] Y. Wang, H.-C. Huang, and X. Jian, "Novel design of a dual-band 5G mm-wave antenna array integrated with a metal frame of a cellular phone," in *Proc. Asia–Pacific Microw. Conf. (APMC)*, Nov. 2018, pp. 1582–1584.

[24] H.-C. Huang, Y. Wang, and X. Jian, "Novel integrated design of dual-band dual-polarization mm-wave antennas in non-mm-wave antennas (AiA) for a 5G phone with a metal frame," in *Proc. Int. Workshop Antenna Technol. (iWAT)*, Mar. 2019, pp. 125–128.

[25] J. Kurvinen *et al.*, "Electrically invisible feed lines for mobile devices," *IEEE Trans. Antennas Propag.*, to be published.

[26] M. A. Al-Tarifi, D. E. Anagnostou, A. K. Amert, and K. W. Whites, "Bandwidth enhancement of the resonant cavity antenna by using two dielectric superstrates," *IEEE Trans. Antennas Propag.*, vol. 61, no. 4, pp. 1898–1908, Apr. 2013.

[27] M. A. Al-Tarifi, D. E. Anagnostou, A. K. Amert, and K. W. Whites, "Bandwidth enhancement of the cavity resonance antenna (CRA) using multiple dielectric superstrate layers," in *IEEE MTT-S Int. Microw. Symp. Dig.*, Jun. 2011, pp. 1–4.
[28] L. Martin, E. M. Cruz, B. Froppier, and T. Razban, "New heterogeneous superstrate high gain antenna," in *Proc. 9th Eur. Conf. Antennas Propag. (EuCAP)*, Apr. 2015, pp. 1–5.
[29] H. Vettikalladi, O. Lafond, and M. Himdi, "High-efficient and high-gain superstrate antenna for 60-GHz indoor communication," *IEEE Antennas Wireless Propag. Lett.*, vol. 8, pp. 1422–1425, 2009.
[30] A. Pirhadi, H. Bahrami, and J. Nasri, "Wideband high directive aperture coupled microstrip antenna design by using a FSS superstrate layer," *IEEE Trans. Antennas Propag.*, vol. 60, no. 4, pp. 2101–2106, Apr. 2012.
[31] N. Alexopoulos and D. Jackson, "Fundamental superstrate (cover) effects on printed circuit antennas," *IEEE Trans. Antennas Propag.*, vol. 32, no. 8, pp. 807–816, Aug. 1984.
[32] H. K. Kan, A. M. Abbosh, R. B. Waterhouse, and M. E. Bialkowski, "Compact broadband coplanar waveguide-fed curved quasi-yagi antenna," *IET Microw., Antennas Propag.*, vol. 1, no. 3, pp. 572–574, 2007.
[33] W. R. Deal, N. Kaneda, J. Sor, Y. Qian, and T. Itoh, "A new quasi-yagi antenna for planar active antenna arrays," *IEEE Trans. Microw. Theory Techn.*, vol. 48, no. 6, pp. 910–918, Jun. 2000.
[34] H. K. Kan, R. B. Waterhouse, A. M. Abbosh, and M. E. Bialkowski, "Simple broadband planar CPW-fed quasi-yagi antenna," *IEEE Antennas Wireless Propag. Lett.*, vol. 6, pp. 18–20, 2007.
[35] P. Wu, Z. Wang, and Y. Zhang, "Wideband planar balun using microstrip to CPW and microstrip to CPS transitions," *Electron. Lett.*, vol. 46, no. 24, pp. 1611–1613, 2010.
[36] P. T. Nguyen, A. Abbosh, and S. Crozier, "Ultra-wideband balun using microstrip to slotline transitions," in *Proc. IEEE Asia–Pacific Conf. Antennas Propag.*, Aug. 2012, pp. 309–310.
[37] Y. Qian and T. Itoh, "A broadband uniplanar microstrip-to-CPS transition," in *Proc. Asia–Pacific Microw. Conf.*, vol. 2, Dec. 1997, pp. 609–612.

Resti Montoya Moreno was born in Albacete, Spain, in 1992. He received the B.Sc. (Tech.) degree in telecommunications engineering from the Universitat Politècnica de València, Valencia, Spain, in 2014, and the M.Sc. (Tech.) degree (Hons.) in electrical engineering from Aalto University, Espoo, Finland, in 2016, where he is currently pursuing the D.Sc. (Tech.) degree.

He was a Research Assistant with Aalto University before joining Intel as an RF Engineer Intern in 2016. Since 2017, he has been a Doctoral Candidate with Aalto University. His current research interest includes 5G and mm-wave antennas for base stations and mobile devices.

Juha Ala-Laurinaho received the Diploma Engineering (M.Sc.) degree in mathematics and the D.Sc. (Tech.) degree in electrical engineering from the TKK Helsinki University of Technology, Espoo, Finland, in 1995 and 2001, respectively.

He has been with TKK, currently Aalto University, serving in the Radio Laboratory from 1995 to 2007, in the Department of Radio Science and Engineering from 2008 to 2016, and currently with the Department of Electronics and Nanoengineering. Currently, he works as a Staff Scientist. He has been a Researcher and a Project Manager in many millimeter-wave technology-related projects. His current research interests are the antennas and antenna measurement techniques for millimeter- and submillimeter-waves, and the millimeter-wave imaging.

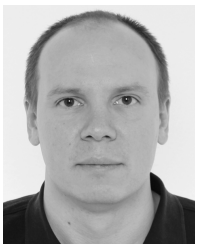

Alexander Khripkov (Member, IEEE) received the B.S. degree in radio engineering and the Ph.D. degree in antennas and microwave devices from the Southern Federal University of Russia, Rostov-on-Don, Russia, in 2002 and 2007, respectively.

From 2007 to 2012, he was a Researcher with the Department of Ultra-Wide Band Sensors for Medical Applications, Industrial Technology Research Institute, Taipei, Taiwan. From 2012 to 2016, he was a Group Leader of the Electromagnetic Solutions Group, Samsung Research and Development Institute, Moscow, Russia. He is currently a Principal Antenna Engineer with the Terminal Antenna and RF Laboratory, Huawei Technologies, Helsinki, Finland. He has authored or coauthored about 30 articles in peer-reviewed journals and conference proceedings, and holds eight granted U.S. patents and about 20 granted patents in other countries. His current research interests include microwave/millimeter-wave antennas and circuits, millimeter-wave systems, terminal antennas, reconfigurable antenna arrays, and metamaterial-inspired structures.

Dr. Khripkov was a recipient of over ten industrial awards. He serves as a reviewer for more than 20 journals in the IEEE Antennas and Propagation Society and the *IET Communications*.

Janne Ilvonen was born in Helsinki, Finland, in 1976. He received the M.Sc. and Lic.Sc. degrees (Hons.) and the D.Sc. (Tech.) degree in electrical engineering from Aalto University, Espoo, Finland, in 2009, 2012, and 2014, respectively.

From 2015 to 2016, he was a Senior Antenna Engineer with Microsoft Mobile, Espoo, where he developed antenna concepts for Microsoft's future flagship handsets. Since 2016, he has been a Principal Antenna Engineer with Huawei Technology, Helsinki. His current research interest includes sub-6 GHz and mm-wave 5G handset antennas.

Ville Viikari (Senior Member, IEEE) was born in Espoo, Finland, in 1979. He received the Master of Science (Tech.) and Doctor of Science (Tech.) (Hons.) degrees in electrical engineering from the Helsinki University of Technology (TKK), Espoo, Finland. in 2004 and 2007, respectively.

From 2001 to 2007, he was with the Radio Laboratory, TKK, where he studied antenna measurement techniques at submillimeter wavelengths and antenna pattern correction techniques. From 2007 to 2012, he was a Research Scientist and a Senior Scientist with the VTT Technical Research Centre, Espoo, where his research included wireless sensors, RFID, radar applications, MEMS, and microwave sensors. He is currently an Associate Professor and the Deputy Head of the Department with the School of Electrical Engineering, Aalto University, Espoo. His current research interests include antennas for mobile networks, RF-powered devices, and antenna measurement techniques.

Dr. Viikari was a recipient of the Young Researcher Award of the Year 2014, presented by the Finnish Foundation for Technology Promotion, the IEEE Sensors Council 2010 Early Career Gold Award, the 2008 Young Scientist Award of the URSI XXXI Finnish Convention on Radio Science, Espoo, and the Best Student Paper Award of the Annual Symposium of the Antenna Measurement Techniques Association, Newport, RI, USA, from October 30 to November 4, 2005. He has served as the Chair of the Technical Program Committee of the ESA Workshop on Millimetre-Wave Technology and Applications and the Global Symposium on Millimeter Waves (GSMM) twice, in 2011 and 2016, in Espoo.